14

LIDAR Atmospheric Sensing by Metal Vapor and Nd:YAG Lasers

Dimitar Stoyanov, Ivan Grigorov, Georgi Kolarov,
Zahary Peshev and Tanja Dreischuh
Institute of Electronics, Bulgarian Academy of Sciences, Sofia
Bulgaria

1. Introduction

LIDAR systems have widely been used for remote investigation of atmospheric parameters (Measures, 1984; Kovalev & Eichinger, 2004; Weitkamp, 2005). They are based on the so-called LIDAR (LIght Detection And Ranging) principle which consists in sending a laser pulse to the atmosphere and subsequent detecting of the radiation backscattered (at angle π) by atmospheric constituents or pollutants. As LIDAR is a time-of-flight technique, the return signal profile detected in the time domain contains range-resolved information about the atmospheric characteristics along the line of laser beam propagation. Advantages of the lidar measurement approaches, as compared to other available active techniques (e.g. radars), are the high spatial and temporal resolution, higher sensitivity and accuracy in sensing atmospheric particles, covering large observation areas, etc. These features make lidar systems powerful instruments for environmental measurements. At present, lidars find a variety of applications in different fields of the human activity. Along with the meteorology, atmospheric physics, and ecological monitoring, lidars are extensively used for volcanic and fire alerting, laser ranging, altimetry and bathymetry, lidar mapping and forestry, coastal morphology and hazards assessment in geology, as well as for many other applications in physics and astronomy, nuclear fusion, military, aviation, robotics, transportation, etc. There exists a variety of ground-based, air-borne and space-borne lidar systems distinguished by their types, schematics, regimes of operation, monitored parameters, constructions, etc. (Kovalev & Eichinger, 2004; Weitkamp, 2005). Among the most widely used systems are the one- or multi-wavelength aerosol lidars exploiting elastic scattering of light.

The present chapter describes the capabilities of LIDAR sensing techniques for atmospheric aerosol profiling by using elastic-scatter lidars based on metal vapor (MV) lasers, as well as on Nd:YAG lasers. First, a brief overview of the basic principles of the LIDAR remote sensing of the atmosphere is given. The single-scattering equations connecting return signal profiles, parameters of the experimental system and characteristics of the probed aerosols along the laser beam are presented in Sec.2, as well as some theoretical approaches for solving the lidar equations in the case of non-absorbing atmosphere (aerosol and molecular). General lidar schematics and methods for detection of lidar signals are also discussed. Special attention is paid to metal vapor and Nd:YAG lasers (Sec.3), and to advantages of

using them in the lidar remote sensing of the atmosphere (Sec.4). Then, in Sec.5, a number of experimental results on lidar atmospheric sensing, obtained with these systems are presented. Reported are measurements focused on evaluations and range resolved profiling of a defined set of important optical characteristics of the atmospheric aerosol, such as backscattering and extinction coefficients, Ångström exponent, etc., as averaged over time so in their temporal evolution. This is in view of the close relation of these characteristics to the spatial distribution, concentration, size parameters, and dynamics of the atmospheric aerosol content. Also, the use of lidars for ecological measurements and detection of hidden aerosol pollution transport by lidar mapping, including the trans-border pollution transport over the Danube River, is shown. Special consideration is given to applications concerning remote sensing of different atmospheric phenomena such as volcanic ash and Saharan dust, to parallel observations with space-borne lidars, etc. In Sec.6, the role of multi-wavelength aerosol lidar probing in the mid-visible and near infrared (IR) ranges is underlined, as a powerful and reliable approach for atmospheric observations providing accurate range-resolved profiling of valuable atmospheric parameters with high spatial and temporal resolution.

2. LIDAR atmospheric sensing

LIDAR remote sensing of the atmosphere represents a complex activity joining together a variety of experimental equipments, measurement techniques, analytical methods, theoretical approaches, etc. Lidar sensing process includes the following principal stages:

- Emitting pulsed radiation into atmosphere;
- Receiving, detection, and recording of backscattered lidar signals;
- Lidar signal conversion and preprocessing;
- Data processing and profiling of major parameters of interest;
- Displaying, visualization, analysis and interpretation of obtained results.

The interpreted results from the lidar sensing can be used by different authorities (governmental, local, etc.) for decision making.

2.1 General lidar block-schematic

Regardless of the mentioned above diversity of lidars, there are some basic components common for all the systems, such as transmitter, receiver, and acquisition subsystems. A general block-diagram of a lidar is presented in Fig.1. One of the main parts of the lidar is the laser transmitter emitting pulsed radiation of appropriate power, spectral, spatial, and temporal characteristics. The laser beam is transmitted into the atmosphere by an opto-mechanical set-up. The latter comprises a set of optical elements (mirrors, splitters, etc.) for laser beam transportation and time-synchronization, an expanding telescope for minimising the output beam divergence, and mechanical mounts with precise translation and rotation mechanisms for beam steering and lidar adjustment.

The lidar receiver consists of optical receiving part and photo-electronic blocks. Backscattered radiation is collected by a telescope. Refractive and reflective telescopes of different types (Cassegrain, Newtonian, Schmidt, etc.), size, and configurations are typically used. A changeable properly-shaped and sized field-stop diaphragm, placed near the focal

point of the telescope, provides angular spatial filtering of the backscattered radiation, forming by this manner the telescope's field of view in conformity with the laser beam divergence. An important part of the multiwavelength lidar receivers is the optical module for wavelength- and/or polarization separation and discrimination. It represents an optical assembly containing dichroic beam-splitters forming the lidar spectral channels for initial wavelength separation of the backscattered laser radiation. Narrow bandpass (1-3 nm FWHM) interference filters are usually placed in each of the spectral channels, providing the main fine spectral selection of the corresponding wavelengths and suppressing the solar radiation background, especially in day-time measurements. Residuals from the other laser wavelengths are further suppressed by using additional spectrally-selective optical elements (e.g. edgepass filters), leading to final transmission of less than 10^{-4}% in the blocking spectral regions. As a result, a good enough signal-to-noise ratio is normally achieved, allowing reliable detection of weak lidar signals and, hence, reaching high altitudes of lidar sounding. Lidar spectral channels can be equipped for measurement of the depolarization ratio of aerosol backscatter on defined wavelengths as it is important for aerosol particle shape characterization.

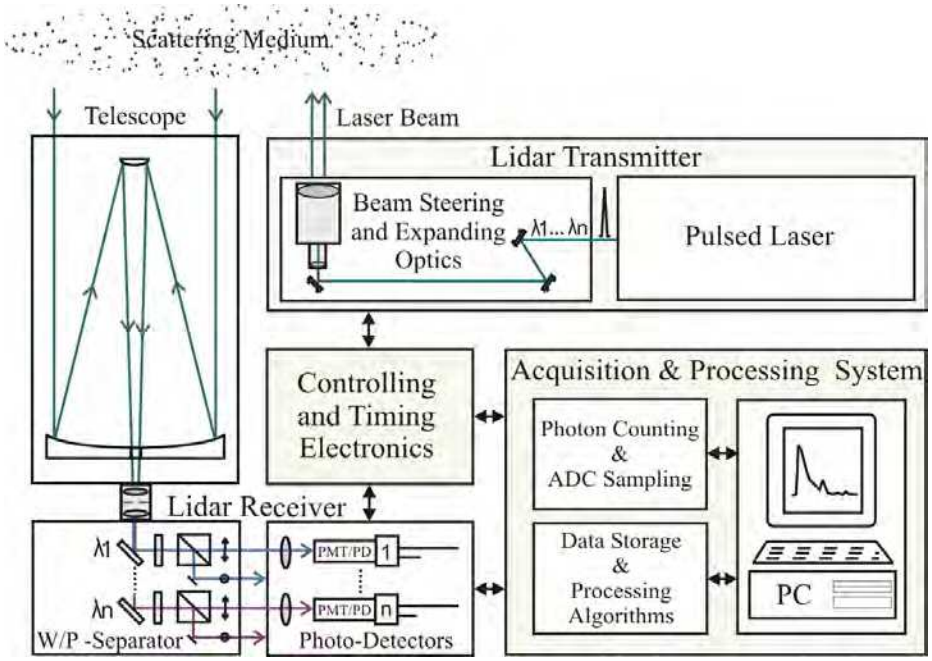

Fig. 1. General block diagram of a lidar system.

Spectrally selected optical lidar signals are detected and converted to electrical ones by using highly-sensitive photodetectors such as photomultipliers, avalanche photodiodes, and CCD-cameras. Further, the received signals enter the acquisition system which provides sampling and pre-processing of raw signals to standard lidar data. The acquisition system is designed to operate in either analog or photon-counting modes, depending on the lidar type, laser pulse energy, measurement tasks, etc. The acquired lidar profiles are stored and

processed by specialized retrieving algorithms and software. The controlling and timing electronics provides the overall lidar operation.

2.2 Lidar equation

Basic aerosol parameters derived from lidar data are the aerosol backscattering and extinction coefficients. Theoretical models for retrieving their range profiles from raw lidar data are based on solving of so-called lidar equation describing the relation between the received range-resolved backscattered optical radiation power and atmospheric and system parameters. For a single-scattering elastic backscatter lidar (measuring backscattered light at the same wavelength as the sensing laser wavelength λ) the power $P(r)$, detected at a time t after the instant of pulse emission, is written as:

$$P(r) = P_0 \frac{c\tau}{2} A\varepsilon \frac{\gamma(r)}{r^2} \beta(r) \exp\left[-2\int_0^r \alpha(\rho)d\rho\right], \tag{1}$$

where $r=ct/2$ is the distance along the laser beam path, P_0 is the average power of a single laser pulse, τ is the pulse duration, A is the area of the primary receiving optics, ε is the overall system efficiency, $\beta(r)$ and $\alpha(r)$ are the backscattering and extinction coefficients, respectively, at wavelength λ. The term $\gamma(r)$ describes the overlap between the laser beam and the receiver field of view, being equal to 1 for ranges of complete overlap. To solve the lidar equation (1), it is useful to split the backscatter and extinction in molecular and aerosol terms:

$$\beta(r) = \beta_a(r) + \beta_m(r); \quad \alpha(r) = \alpha_a(r) + \alpha_m(r). \tag{2}$$

In Eq.(2) and further, the subscripts "a" and "m" stand for aerosol and molecular terms, respectively. We also assume negligible atmospheric absorption at a wavelength λ and $\gamma(r) = 1$. In next step we introduce the aerosol extinction-to-backscatter lidar ratio $S_a(r)$ as:

$$S_a(r) = \alpha_a(r) / \beta_a(r) \tag{3}$$

by analogy with the molecular extinction-to-backscatter ratio:

$$S_m = \alpha_m(r) / \beta_m(r) = 8\pi / 3. \tag{4}$$

$S_a(r)$ depends on range r through the size distribution, shape, and chemical composition of the aerosol particles. Substituting Eqs.(2) in Eq.(1), and bearing in mind Eqs.(3) and (4) , we obtain:

$$\begin{aligned} &P(r)r^2 \exp\left\{-2\int_0^r [S_a(\rho) - S_m]\beta_m(\rho)d\rho\right\} = \\ &= P_0 C[\beta_a(r) + \beta_m(r)] \exp\left\{-2\int_0^r [\beta_a(\rho) + \beta_m(\rho)]S_a(\rho)d\rho\right\} \end{aligned}. \tag{5}$$

In Eq.(5) the constant $C=A\varepsilon c\tau/2$ (so-called lidar constant) covers all system parameters. Next, following the steps described in Weitkamp, (2005), we take the logarithm of both sides of Eq.(5) and differentiate it with respect to r. Finally a differential equation of Bernoulli type is obtained. In a case when the values $\beta_a(r_0)$ of aerosol and $\beta_m(r_0)$ of molecular backscattering

at a reference range r_0 are known, the lidar can be calibrated with these boundary conditions to determine the calibration constant P_0C. Then the solution of Eq.(5) can be written as follow:

$$\beta_a(r) = -\beta_m(r) + \frac{P(r)r^2 \exp\left\{-2\left[S_a(r) - S_m\right]\int_{r_0}^{r} \beta_m(\rho)d\rho\right\}}{\frac{P(r_0)r_0^2}{\beta_a(r_0) + \beta_m(r_0)} - 2\int_{r_0}^{r} S_a(\rho)P(\rho)\rho^2 \exp\left\{-2\left[S_a(\rho) - S_m\right]\int_{r_0}^{\rho} \beta_m(\rho')d\rho'\right\}d\rho}. \quad (6)$$

The molecular atmospheric backscattering coefficient $\beta_m(r)$ can be determined from the model of Standard atmosphere or calculated using meteorological data from a radiosonde. However, the aerosol backscattering $\beta_a(r)$ and extinction $\alpha_a(r)$ [or the aerosol lidar ratio $S_a(r)$], remain to be determined as two unknown variables from the values of one variable – the so-called range corrected signal $P(r)r^2$, obtained from the lidar measurement. This is not possible without using additional information about at least one of the unknown variables. When choosing the reference range r_0 near to the ground (and to the lidar), the aerosol backscattering $\beta_a(r_0)$ or extinction $\alpha_a(r_0)$ can be measured independently. After that, we can integrate Eq.(6) and retrieve the atmospheric backscattering coefficient profile. Unfortunately, there exists a mathematical instability in the calculations following Eq.(6) in sense that small errors in the determination of $\beta_a(r_0)$ at the reference distance r_0 or in the measured range corrected signal $P(r)r^2$, start to produce in few steps of integration procedure negative values for the denominator and, consequently, for $\beta_a(r)$. To solve this problem, Klett (Klett, 1981) and Fernald (Fernald, 1984) proposed an inverse integration of Eq.(6), starting from the far end of the lidar sounding path. Applying this idea and introducing $\beta_a(r_{\max}) = \beta_a^{\max}$ and $\beta_m(r_{\max}) = \beta_m^{\max}$, where r_{max} is the maximal distance, we can rewrite Eq.(6) as follows:

$$\beta_a(r) = -\beta_m(r) + \frac{P(r)r^2 \exp\left\{-2\left[S_a(r) - S_m\right]\int_{r}^{r_{\max}} \beta_m(\rho)d\rho\right\}}{\frac{P(r_{\max})r_{\max}^2}{\beta_a^{\max} + \beta_m^{\max}} + 2\int_{r}^{r_{\max}} S_a(\rho)P(\rho)\rho^2 \exp\left\{-2\left[S_a(\rho) - S_m\right]\int_{\rho}^{r_{\max}} \beta_m(\rho')d\rho'\right\}d\rho}. \quad (7)$$

The reference range r_{max} is chosen so that the aerosol backscatter coefficient is negligible compared to the molecular backscatter coefficient, i.e. $\beta_a(r_{max}) << \beta_m(r_{max})$. Normally such atmospheric conditions are observed in the upper troposphere. Thus, we can attach the upper backscattering value to the value of the molecular backscattering and calculate the backscatter profile in backward direction by Eq.(7), using the measured range-corrected lidar signal. Determination of the reference range r_{max} is a problem for some atmospheric conditions as cloudy atmosphere, intensive background, etc. (see Sec.6). This algorithm is now widely applicable in practice, assuming also invariant value for the aerosol lidar ratio S_a=const along the laser beam path in the atmosphere. The exact value of this constant is determined depending on the laser wavelength and also on *a priori* assumptions about the type of the observed aerosols. The influence of the assumption for constant aerosol lidar ratio on the results of calculated profiles of atmospheric backscattering coefficient is studied

and described in Böckman et al., 2004. The backscattering profiles are calculated from numerical models of lidar returns in two stages: once using constant $S_a(r)$, and second – with variable profile of $S_a(r)$. As shown, the errors in the calculated aerosol backscatter profiles due to the variance of the aerosol lidar ratio at different atmospheric conditions could reach 25-30%. The conclusion thrusts on the strong recommendation to use all available *a priori* information about the atmospheric conditions and the observed aerosols to apply an adequate variable aerosol lidar ratio in lidar determination of the aerosol backscatter profiles.

2.3 Photon detection methods in lidar sensing

Photon detection (using photomultipliers, photodiodes, etc.) is a key operation in optical devices, including lidars (Gagliardi & Karp, 1976). The understanding of photon detection processes is of essential importance for the development and performance of the lidar. This process is described by the probability for a photoelectron emission, which is proportional to the square of the envelope of the classical electromagnetic field (the optical field intensity) on the photosensitive surface. The transformation of optical field into a photoelectron flux is a quantum process. The output photoelectron current is a random temporal process, corresponding to the random photon absorption by independent quantum systems of the photocathode and to the photoelectron emission. The concept for the randomness of the photoelectron current is always valid for the stochastic or determined optical fields. The output photoelectron current $I_{phe}(t)$ is described mathematically by a superposition of δ-pulses, each corresponding to a single process of photoelectron emission or

$$I_{phe}(t) \sim \sum_{k=1}^{N(0,t)} \delta(t - t_{phe,k}), \tag{8}$$

where k=1,…,$N(0,t)$ are the successive photoelectron numbers, $N(0,t)$ is the total number of photoelectrons and $t_{phe,k}$ are the so-called photoelectron arrival times. As seen, the information, carried by the optical field after the photodetection, is contained in the arrival times of photons (or photoelectrons). As the probability of photoelectron emission depends on the optical intensity, the increase of optical energy causes an increase of the number of photoelectrons per unit time and thus, decreasing the time intervals between adjacent photoelectrons. This is the so-called effect of photoelectron time-grouping, depending on the instant optical intensity. The optical field is transformed into a photoelectron flux of time-dependent intensity. Measuring the arrival times $t_{phe,k}$ of all photoelectrons one could, in principle, extract the whole information carried by the optical field.

Different effects in photon detectors prevent the extraction of the entire information from the received optical radiation. The output current $I_{out}(t)$ can be expressed now in the form:

$$I_{out}(t) \sim \sum_{k=1}^{N(0,t)} h_k(t - t_k), \tag{9}$$

where $h_k(t\text{-}t_k)$ are the output pulse functions of finite duration, depending on the photon detector parameters. They are usually called single electron pulses (SEPs) or photoevents. The SEPs are of fluctuating shapes, amplitudes, and arrival times t_k. The electric charge G_k of an individual k-th SEP is a fluctuating variable, depending mainly on the processes of the secondary emission. It is given by

$$G_k \sim q\int_{-\infty}^{\infty} h_k(t-t_k)dt\,, \tag{10}$$

where q is the electron charge. The SEP arrival times are expressed by $t_k=t_{phe,k}+t_{pd}+\Delta t_k$, where t_{pd} is the mean time delay and Δt_k are the centered time delay fluctuations or the jitter (transit time spread) of the photon detector. The mean time width τ_{pd} of the SEPs defines the receiving frequency bandwidth $\Delta\omega_{pd}\sim\pi/\tau_{pd}$ of the photon detector.

The parameters of $h_k(t\text{-}t_k)$ dramatically affect the photoreceiving process. It becomes impossible to measure the photoelectron arrival times at the photon detector output. It is due mainly to limitations imposed by the processing electronics. The temporal structure of the output current $I_{out}(t)$ provides successive extraction of the optical information from the flow of SEPs at the output in definite number of cases, strongly depending on the optical intensity. Four basic regimes (modes) of photodetection are typically recognized, requiring specific approaches to be applied in developing optical receivers and corresponding acquisition techniques. An approximate criterion for distinguishing these regimes is the number of photoevents (or SEPs) per the photon counter dead time τ_{dead} [as a rule $\tau_{dead}>(3-5)\tau_{pd}$]. Its appearance is due to the carrier restoration processes in transistors and diodes of electronic circuits after the photon detector (discriminators, amplifiers, etc). The dead time prevents the registration of two successive SEPs, separated by time intervals, shorter than τ_{dead}, causing nonlinearities in the detection process. The quoted above photodection modes (ordered by increasing of optical intensity) are as follows: single quantum (SQ) mode; photon counting (PC) mode; overlapping (OV) mode; and analog mode (see Fig.2).

In the so-called SQ mode, the time intervals between adjacent SEPs are quite larger than the dead time and, thus, the probability for appearance of adjacent SEPs, separated by intervals of the order of τ_{dead}, is minimized. This condition provides the measurement of individual arrival times of SEPs. Unfortunately, photon rates in this mode are very low, resulting in intolerably long accumulation times in many applications including the lidar sensing.

The photon counting is realized by conversion of SEPs into corresponding normalized electric pulses of standard amplitude (NSEPs) (photocounts). This transformation just causes the dead time effects. The normalized pulses are then counted (within some defined sampling intervals Δt) by standard electronic circuits. To count the normalized SEPs (i.e., to count photons) they have to be resolved in time. It is evident that minimum time intervals between the adjacent SEPs have to be longer than the dead time τ_{dead}. The maximum tolerable instantaneous photon count rate R_{NSEP} (in number of NSEPs per second) can be estimated approximately by the condition $(R_{\mathrm{NSEP}})_{\max}\tau_{dead}\le 1$. Because of the time grouping effects of photoevents, a part of input SEPs will not be counted, if $(R_{\mathrm{NSEP}})_{\max}\tau_{dead}\sim 1$. That is why the values of $(R_{\mathrm{NSEP}})_{\max}\tau_{dead}\le 0.1$ are more preferable to be satisfied in photon counting receivers in order to provide linear dependence of the counted NSEPs on the input optical intensity. The NSEPs are described by Poisson statistics as it is for the input photon flux. The dynamic range of PC receiver is very high. At higher intensities it is limited by the above condition $(R_{\mathrm{NSEP}})_{\max}\tau_{dead}\sim 1$. However, there are no limitations at low intensities. The only limitation here is the tolerable data accumulation (measurement) time. For these reasons the PC mode is widely used in modern lidar systems.

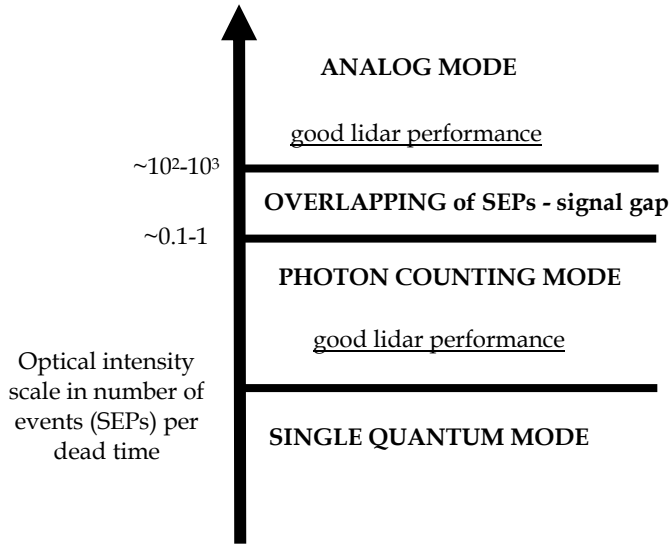

Fig. 2. Regimes of photon detection as a function of optical intensity.

The overlapping mode is typically recognized as a non-operational signal gap, where the performance of optical receivers is ineffective. In OV mode the output flow of SEPs (before the normalization) could be represented by a stochastic process, due to the random summation (at each moment) of a low number of SEPs of fluctuating individual charges, shapes, duration, and arrival times. The output current is not proportional to the optical intensity. The appearance of OV mode is due mainly to the electronics, when the photon counts are not resolved any more (due to the higher photon rates) in order to be counted. At the same time, due to the large fluctuations of the output amplitudes, signals could not be correctly sampled by analog-to-digital converters (ADCs). In OV mode the input optical intensity is higher than that in PC mode and this is why the OV mode is attractive for development of methods for providing the linear performance. Some novel techniques are reported (Stoyanov, 1997; Stoyanov et al., 2000). The analysis of OV mode is out of the scope of this chapter as it is not used in lidar sensing.

The analog mode is a basic regime of optical receiving (together with PC mode), widely used in lidar sensing. Here the number of SEPs at the photon detector output typically exceeds 10^2-10^3. In this mode, the fluctuations of SEP parameters can be neglected because of the averaging over a large number of SEPs at each moment. The output current is an analog signal of amplitude proportional to the input intensity and can be directly sampled by ADCs. The noises in the output current typically also display Poisson statistics, but because of the larger number of photons within each sampling interval it is transformed into Gaussian one.

The analog and PC regimes of optical detection impose special requirements to the lasers, used in lidars. Say, the analog mode is typically used with high pulsed power, low repetition rate lasers (as Nd:YAG lasers). The Nd:YAG lidars are also used in PC mode for large distances for which the number of received photons dramatically decreases. Here the

measurement times are normally higher, due to the lower return intensities. In practice, the combined use of both regimes causes some problems as the gluing of both lidar profiles. The PC mode in lidar sensing can also be realized by lasers of lower pulsed power but at higher pulse repetition rates, providing high enough mean output power. In this case the above requirements to PC mode can be satisfied.

Assuming Poisson statistics (Sec.2.3) for the photon detector output signal fluctuations, the probability $W_{N(r)}$ of detecting $N(r)$ photons (or SEPs) from a distance r in PC and analog modes for a sampling interval Δt at a mean rate R_N is given by :

$$W_{N(r)} = (R_N \Delta t)^{N(r)} (N(r)!)^{-1} \exp(-R_N(r)\Delta t) . \quad (11)$$

For Poisson distributed lidar signals the noise variance $\sigma_N^2(r)$ is determined from the mean number of detected photons (SEPs) per sampling interval by the expression $R_N(r)\Delta t = \sigma_N^2(r)$. The contribution of Poisson noises with variance $\sigma_N^2(r)$ is essential in the total error balance of lidar measurements. Unfortunately, as it is clear from the lidar equation (Sec.2.2), a multitude of variables contribute to the total estimated error. In fact it is difficult to find an analytical expression for the errors of the calculated backscatter profiles by a classical way, differentiating the lidar equation. In the practice a roundabout approach is applied. It consists in two-step calculation of the backscatter coefficient profiles: i) using the measured values of the range corrected signal $P(r)r^2$; ii) adding some estimated deviation to the measured values $P(r)r^2 \pm \sigma_E(r)$, where $\sigma_E(r) \geq \sigma_N(r)$ is the estimated deviation profile. If no other useful information is available to estimate strictly $\sigma_E(r)$, at least the Poisson variance $\sigma_N(r)$ of lidar signals can be added for estimation of lower error limit and the error propagation along the backscatter calculus chain.

3. Metal vapor and Nd:YAG lasers: Basic parameters

The requirements for successful lidar atmospheric sensing impose strong limitations on the laser parameters as the pulse width, pulsed and mean powers, repetition frequency, operational wavelengths, stability, etc. That is why the number of laser types applied in lidars is limited. The Nd:YAG lasers are widely used in the most of lidar systems (Measures, 1984; Weitkamp, 2005) providing simultaneous sensing in analog and photon counting modes at typically 4 to 6 wavelengths (using harmonic generation techniques) in the IR, visible and near UV ranges (including Raman channels). Lasers emitting a set of basic wavelengths of proper parameters, say approximately equal output powers, are also of great importance for multiwave lidar atmospheric sensing. The use of such lasers can simplify the opto-mechanical lidar design.

The MV lasers eligible for lidar probing (in the sense of above requirements) are mainly lasing on two active media, namely copper (Cu) and gold (Au) vapors. They offer unique output parameters (Astadjov et al., 1988; Kim, 1991; Stoilov et al., 2000) attractive for development of lidars in the mid-visible range, capable to probe simultaneously the troposphere and stratosphere. These lasers emit pulses with mean power of up to 2 kW at relatively high repetition frequencies, normally ranging from 2 KHz to 100 KHz, depending on the laser type. The pulsed energy is substantially low (~0.1 mJ at 5-10 ns pulse duration). The combination of low pulse energy, high mean power, high repetition frequency and multiwavelength performance of MV lasers are their key advantages for application in lidar

remote sensing. Typically, output powers of 1-3 W are sufficient for probing simultaneously the troposphere and stratosphere.

Most of the available Cu-vapor lasers operate using one of the two active substances - pure Cu or CuBr. They emit two basic spectral lines (at 510.6 nm and 578.2 nm) of close mean output powers. The beam and temporal characteristics at both lines are practically equal. These lasers provide Gaussian beams of low intensity fluctuations and simultaneous emission of pulses at both wavelengths. The CuBr lasers are more preferable for lidars, because of their very low readiness time (~5-15 min), due mainly to the quite lower working temperature of about 450 ^{0}C as compared to 1500 ^{0}C -1700 ^{0}C for lasers on pure Cu.

Lasers on Au-vapor emit radiation basically at a wavelength of 627.8 nm with temporal and beam parameters quite similar to these of pure Cu-vapor lasers. The combination of Cu- and Au-vapor lasers in a single laser tube is very attractive for lidar applications. Mean output powers of ~0.5 W for each of the three lines 510.6 nm, 578.2 nm and 627.8 nm will be sufficient to cover heights above 15 km in PC mode.

Conventional flashlamp-pumped Nd:YAG lasers, operating in Q-switching mode, provide pulses of 5-10 ns FWHM, at 10-100 Hz typical repetition rates, with extremely high pulse energy reaching more than 1 J at the fundamental wavelength (1064 nm) and up to hundreds of millijoules at the second (532 nm), third (355 nm), and fourth (266 nm) harmonics. These lasers can be designed for simultaneous operation at all the available wavelengths or at optional combinations of them, being by this manner powerful multi-wavelength sources of UV, visible, and IR light. They exhibit perfect shot-to-shot energy stability (instabilities of ≤±2%), long-term power drift of less than ±3%, and temporal jitter of ≤1 ns. In addition, Nd:YAG lasers possess excellent beam-quality characteristics such as Gaussian spatial profile, beam divergence down to 0.5 mrad, pointing stability of < 50 μrad, and polarization ratio > 80%. Diode-pumped Nd:YAG lasers, using bars of powerful laser diodes instead of flash-lamps, are also commercially available. They combine the features quoted above with compactness and high averaged power at kHz pulse frequencies.

4. Lidars on metal vapor and Nd:YAG lasers

Lidars on metal vapor and Nd:YAG lasers are used since mid 70-ties of the last century. The fast progress in development of Nd:YAG lasers of stable and very good output parameters, meeting the requirements for effective atmospheric probing, provided their wide applications in most of lidar sensing systems. In the first decade of the new century, the problems related to more precise range-resolved characterization of the atmosphere (aerosol and molecular content, clouds, air quality, atmospheric transport, etc.) became the most important challenge to the modern lidar systems and their future effective incorporation in the Global Atmospheric Watch (GAW) networks. An important approach for improving the characterization procedures is the combined use of lidars (and lidar networks) with some other instruments as sun-photometers, microwave (MW) radiometers, in-situ measurements, etc. In spite of the already proven synergy of this approach, the further improvement of the lidar atmospheric characterization remains an important task. In this sense, a possible solution could be the use of multiwave lidar sensing, especially in the visible range. That is because the typical aerosols, loading the troposphere and low stratosphere as dust, volcanic ash, thin clouds, etc., are of submicron and near micron size range. Thus, they are commensurable to the wavelengths in

the visible range. The simultaneous use of laser radiations covering the green-to-red part of visible range can provide better description of the backscattering wavelength dependence on the aerosol particle sizes, especially in multimode size distributions. Efficient sources of radiation in this spectral domain are the mentioned above Cu- and Au- vapor lasers. The combination of lidars based on these lasers with Nd:YAG lidars operated at 1064 nm and 532 nm offers additional advantages to cover practically the mid-visible and near IR ranges, where the absorption effects can be neglected as a rule.

In Arshinov et al., (1983) the application of Cu-vapor lidar for measuring profiles of the atmospheric humidity and temperature is described. The Cu-vapor lidar system is used for detection of stratospheric aerosol layers at heights of up to 28 km (Kolarov et al., 1988). The scattering ratios (aerosol and molecular to molecular) exceeding 1.5 within the height range 22-28 km are measured at the wavelength of 510.6 nm (1-3 W mean power, 5 KHz repetition frequency, 19cm telescope diameter, and 10-100 s accumulation times) with a photon counting system. A complex system, containing Cu-vapor (510.6 nm) and Au-vapor (627.8 nm) lasers, combined with MW and IR radiometers and MW radar is described in Stoyanov et al., (1988). The two lasers are synchronized in time. The output powers are of 1 -3 W at 510.6 nm and 0.5 W at 627.8 nm, at pulse repetition frequencies 5-15 KHz. The experimentally demonstrated operational heights are 30 km for 510.6 nm and 22 km for 627.8 nm at 100 s accumulation times. The short accumulation times provided opportunities for studying some dynamic processes in the lower stratosphere. One of the most important results of these experiments is the demonstration of good lidar performance in the PC mode within the ranges from the planetary boundary layer (PBL) heights (~750 m) up to 30 km in the stratosphere. The first lidar and MW radiometers remote sensing experiment is performed using Cu-vapor laser of parameters as given above (Gagarin et al., 1987). The operational wavelengths of MW radiometers are 0.8 cm and 1.35 cm to be sensitive to the free water in cloud droplets and the water vapor. The measurement accuracy for the brightness temperature is below 0.1 K. The accuracy of determining cloud water content and water vapor is ~ 0.5% and 1%, respectively. In this schematic, the lack of range resolution of the radiometers is compensated by the good lidar resolution. In series of experiments the links between the time variations of the backscattered time-resolved lidar signals and the brightness temperatures at the radiometer wavelength are demonstrated and analyzed.

The aerosol lidar with CuBr-vapor laser developed at Laser Radars Lab of the Institute of Electronics (LRL-IE), Bulgarian Academy of Sciences, is shown in Fig.3a (Grigorov et al., 2010). The CuBr-laser generates pulses at high-repetition frequency of 13 kHz (10 kHz in the upgraded version), with duration of 10 ns at 510.6 nm and 578.2 nm. Laser beam is directed vertically upward. Two Cassegrain telescopes with 15 cm aperture and 2.25 m focal length receive the backscattered radiation at the two wavelengths. A registration in PC mode is applied. Received backscattered lidar signals are stored in the computer by means of a photon counting board providing spatial resolution of 15-30 m, in 1024 samples and averaging time of 1 min. The maximum height is 15 km, limited by the laser pulse repetition frequency. Under daytime conditions, the sounding height decreases to about 4-5 km, due to intensive sky illumination, reducing the signal-to-noise ratio (SNR). Each lidar measurement lasts about 3-4 hours and more. The lidar profiles, integrated over accumulation time of 1 min, are additionally averaged by summation of data from 30 profiles. Thus, the measurement time for each profile amounts to 30 min. The stored data are subsequently processed by Fernald's algorithm, using a program in MATLAB environment, developed in LRL-IE.

(a) (b)

Fig. 3. Photographs of the CuBr-vapor (a) and Nd:YAG (b) laser-based aerosol lidars at LRL-IE involved in the European Lidar Network measurement programs.

The Nd:YAG lidar system of the LRL-IE (Fig.3b) is a 3-channel combined aerosol-Raman lidar (Peshev et al., 2010). The laser provides output pulse energies of up to 1 J at 1064 nm and up to 120 mJ at 532 nm, at a repetition rate of 2-5 Hz, with pulse duration of 15 ns FWHM. The pulse power is of up to 70 MW at 1064 nm and up to 10 MW at 532 nm. The corresponding values of the averaged power for the two wavelengths are of up to 2 W and 0.25 W, respectively. The output beam divergence is of 2.5 mrad (total angle). These performance characteristics of the laser allow one to carry out nighttime and daytime lidar measurements. The optical part of the receiver contains a Cassegrain telescope (35 cm aperture; 2 m focal length) and a 3-channel spectrum-analyzing module based on dichroic beam-splitters, narrowband interference filters (1-3 nm FWHM), edge-pass filters, and neutral densities. The electronic part of the lidar receiving system consists of three compact photo-electronic modules. Each module comprises a photon detector (photomultiplier or avalanche photodiode), 10 MHz/14-bit ADC, high voltage power supply, and controlling electronics. The aerosol lidar channels operate in analog mode with 15 m range resolution. Receiving modules are connected to a computer by high-speed USB ports. The acquisition system is controlled by specialized software providing the accumulation, storage, and processing of lidar data. It allows for evaluating and plotting profiles of range-corrected lidar signals, aerosol backscattering coefficient, and estimation error.

5. Applications of LIDARS for remote atmospheric sensing

Atmospheric aerosols originate from natural and anthropogenic sources such as desert windstorms, forest fires, volcanic eruptions, sea spray, and combustion products of human

activities. Aerosols, having different size distributions and chemical or physical properties, can affect the climate over large regions. Aerosol particles reflect the solar radiation, act as cloud condensation nuclei, modify the scattering properties and lifetime of clouds, influence the precipitation cycles, as well as atmospheric radiative and thermal balance, etc. Ejecting immense amounts of ashes and gases into the atmosphere, active volcanoes can strongly affect for long periods climate, ecology, aviation industry, agricultural activities, and human health over regions of up to global scale. This is why observations and alerting on volcanic aerosols in the atmosphere are of great importance. Lidars can provide real-time sensing of atmospheric aerosols over large areas with high spatial and temporal resolution.

The significance of lidar information, provided by a single lidar station is essentially enhanced if working in a lidar network. Such an idea combines together researches in different lidar networks as EARLINET (http://www.earlinet.org), MPLNET (http://mplnet.gsfc.nasa.gov/), AD-Net (http://www-lidar.nies.go.jp/AD-Net/), etc. The primary goal of the project EARLINET (European Aerosol Research Lidar Network) is the creation of a common database, banding the results of observation of lidar stations located in the European countries (Bösenberg et al., 2003). Main result of such cooperation is the establishment of a quantitative lidar dataset describing the aerosol vertical, horizontal, and temporal distribution, including its variability on a continental scale. Such a dataset could be a comprehensive data source to address the four-dimensional spatio-temporal distribution of aerosols on a global scale (Pappalardo et al., 2010).

Analyses of lidar data require additional information to improve the interpretations of both the type and origin of aerosol layers. Several regional models for simulation and prediction of the dust cycle in the atmosphere have been developed (Kallos et al., 1997; Ozsoy et al., 2001; Nickovic et al.; 2001; Perez et al., 2006a, 2006b). The Dust Regional Atmospheric Model (DREAM) (Nickovic et al.; 2001; Perez et al., 2006a, 2006b) provides reliable operational forecast maps of dust load and concentration in the atmosphere over the North Africa and Euro-Mediterranean region. The model is operated by the Barcelona Supercomputing Center (BSC), (http://www.bsc.es/projects/earthscience/DREAM/). Maps present the cloud coverage, wind directions and speeds, and dust loads. Another source of information about the origin of the aerosol layers offers the HYSPLIT (HYbrid Single-Particle Lagrangian Integrated Trajectory) model (Draxler & Hess, 1998; Draxler & Rolph, 2011). It represents a complete system for computing simple air parcel trajectories to complex dispersion and deposition simulations. The model can be run interactively through the READY system at the site http://www.arl.noaa.gov/HYSPLIT_info.php of the Air Resource Laboratory of NOAA, USA. Calculations of the forward/backward air mass trajectories give a plot of the path passed by the air mass for a chosen time period before arriving to the lidar station location.

The results of lidar applications in the remote sensing of the atmosphere, presented in this Section, are obtained in the LRL-IE using the two elastic backscatter lidar systems described in Sec.4. Some results are reported, concerning lidar mapping of aerosol fields over large industrial zones as one of the important applications of lidars in the regional ecological studies and expertise.

The Sofia lidar station, being one of the stations working in the frame of the EARLINET project, is involved in the following research activities:

- Regular lidar measurements of the atmosphere performed twice weekly;
- Observation of special phenomena, such as unusually high concentrations of aerosols in the troposphere (transportation of mineral dust from Sahara desert over the Mediterranean Sea to Europe, volcanic eruptions, formation of smoke layers resulting from forest or industrial fires, intense photochemical smog, etc.);
- Correlative measurements with space-borne lidars, in the frame of international cooperation.

5.1 Lidar mapping of aerosol pollutions over industrial regions

The monitoring of air pollution distribution over large industrial and urban zones is an important task for improving the quantitative and qualitative estimates of the pollution impact on the environmental conditions. The air pollution transport from local sources is connected with the motion of air masses driven by the wind. The high temporal and spatial resolution of lidar probing and the speed of measurements define the high efficiency of aerosol transport lidar mapping. The opportunity to scan areas of the order of 50-100 km^2 by a single scanning lidar system can provide valuable information for in-depth analysis of the pollution dynamics over broad regions containing a large number of potential local sources.

Results are presented below from a lidar mapping of air pollution distribution and transborder pollution transport over the Danube River in the region of Silistra (Bulgaria) – Kalarash (Romania). The measurements are performed using a scanning CuBr lidar system (λ=510.6 nm) applying photon counting detection. The main lidar parameters are similar to those described in Sec.4. The scanning system provides 1.6^0 scanning step from 0^0 to 360^0 in the horizontal plane with an angular elevation step of 1^0 within the range from -3^0 to 15^0. The scanning lidar is mounted on the roof of a high building located on the hill near the riverside of the Danube River. The total area scanned in successive measurement sessions in order to map different zones as urban and industrial ones, river ports, etc., is of more than 200 km^2. The scanning zone is divided into sectors, separately mapped by the lidar. The integration time at a given angle is chosen to be 1 min, providing maximum sounding distances to more than 12 km in horizontal direction. The measurement time for scanning a 30^0 angular sector is of about 30 min. Under conditions of measurements, one can accept the concept of approximately frozen aerosol fields. Lidar mapping measurements are supported by simultaneous in-situ measurements (including gas analysis) by a specialized transportable laboratory (Mitzev et al., 1995).

The processing of lidar data includes solutions of lidar equation for each angular direction, using the Klett's inversion method and estimation of the volume aerosol extinction coefficient. The latter is converted into aerosol mass concentration, by using our previously derived approximate empirical expression (Mitzev et al., 1995). Finally, the processed data in mass concentration profiles (stored in radial coordinates) are transformed to rectangular coordinates and attached to the geographical map (see Fig.4).

The lidar maps, created from these measurements contain valuable quantitative information about the spatial distribution of aerosol fields as well as their dominated paths of propagation. Fig.4 presents a lidar map of aerosol distribution (dark blue isolines of constant mass concentration) over an area of ~ 70 km^2 (12 km x 6 km). The Danube River and the Lake of Kalarash are displayed in blue. The contours of some geographical objects are given

in red. Parts of urban regions of Kalarash and Silistra are presented in dark orange. The position of the scanning lidar is marked as well. As seen, two main areas of intensive aerosol loadings are well displayed on the lidar map. The upper map area shows the aerosol field distribution in the vicinity of the steel plant near Kalarash. This plant is one of the main pollution sources in the region of the investigation. The obtained lidar maps related to adjacent sectors show that the pollution emitted in this region is transported approximately parallel to the Danube River, probably not crossing the border. The aerosol plume in the mid-part of the image is identified as to be emitted from the cellulose plant located far from the mapped region. The pollution of this plume is supposed to pass through the river. This estimate is supported by the parallel gas analysis. The measured phenol concentration (typical for cellulose manufacturing) exceeds about 8 times the tolerable level in Silistra.

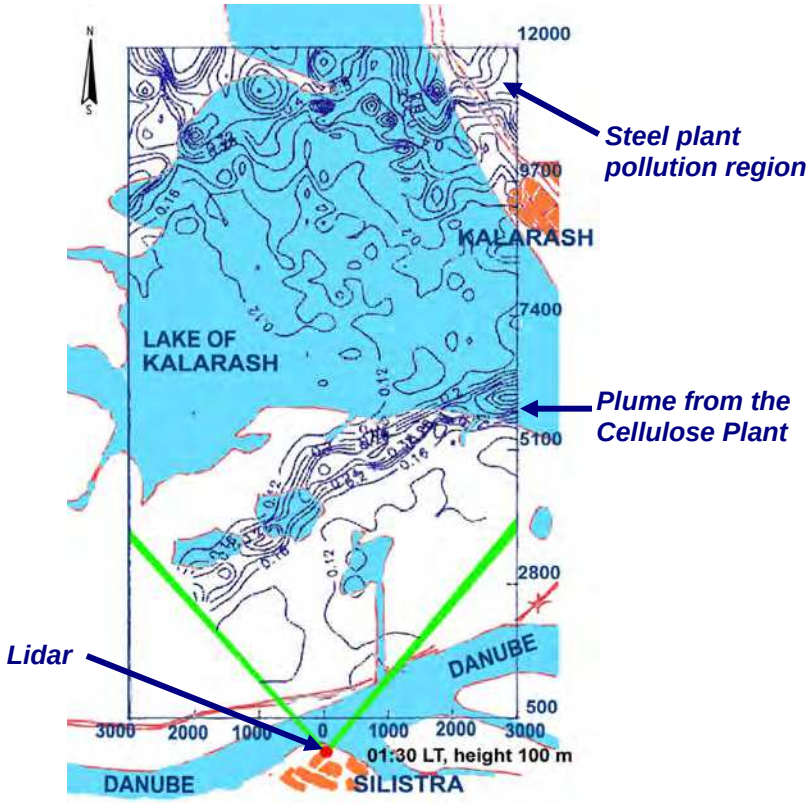

Fig. 4. Lidar map of aerosol pollution distribution over the Silistra – Kalarash region; 14.10.1992.

5.2 Lidar observations on Saharan dust loadings in the atmosphere

Numerous observations on Saharan dust presence in the atmosphere over Sofia are carried out by both lidars of LRL-IE, in order to follow the concentration, spreading, and temporal

evolution of Saharan dust transported over European continent (Papayannis et al., 2008; Grigorov et al., 2009). Measurements are synchronized in time with the BCS-DREAM model forecasts for dust loadings and transport.

As an illustration, vertical profiles of the aerosol backscattering coefficient measured by the Nd:YAG lidar at 1064 nm and 532 nm on 4 November 2010, during a dust-transport event, are presented in Fig.5a. The altitude range 1-5 km above sea level (ASL) is only shown in order to zoom the profile part containing the Saharan dust layer. The latter is located in the range 2.8-4 km ASL, just above the PBL as typically. The color-coded DREAM dust loading forecast map for a time preceding the measurements is displayed in Fig.5c. As one can see on the map, a dust layer with density of about 0.2 g/m^2 has covered the lidar station region, in good correlation with the intense peaks of dust backscattering coefficient (exceeding 1x10^{-6} m^{-1}sr^{-1} at 532 nm) observed in Fig.5a.

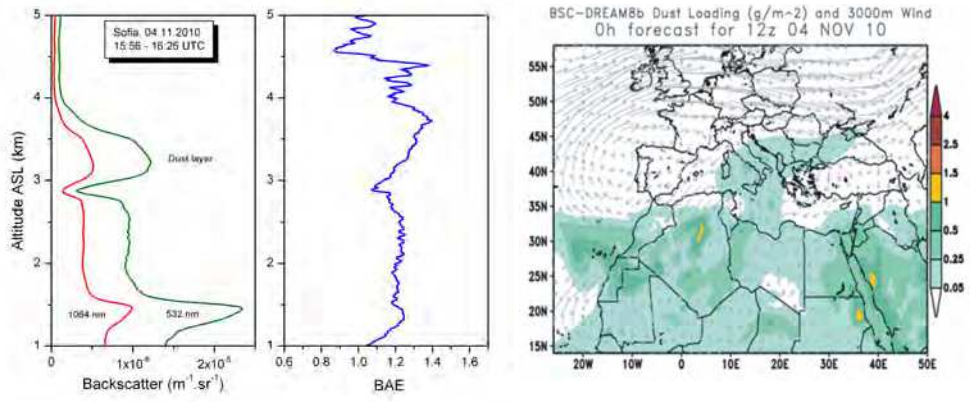

(a) (b) (c)

Fig. 5. Vertical profiles of the aerosol backscatter coefficient at the two lidar wavelengths (a), corresponding profile of BAE (b), and BSC-DREAM forecast map of dust loading (c).

The vertical profile of backscatter-related Ångström exponent (BAE) is shown in Fig.5b, corresponding to profiles in Fig.5a. The BAE values are nearly constant (~1.2) in the underlying PBL. They increase with height reaching 1.3-1.4 just in the dust layer. Such values (1-1.4) are typical for Saharan dust, implying sub-micron dust particle size domination.

Height-time-coordinate diagrams of the backscatter coefficient evolution are presented in Fig.6, as measured in successive time intervals by the CuBr and Nd:YAG lidars at 510.6 nm (a) and 532 nm (b), respectively. As obvious from both diagrams in Fig.6, the Saharan dust layer is well expressed, intense, and relatively stable in terms of height and thickness.

Nevertheless, one can perceive specific internal structure of density distribution evolving over time. The aerosol layer at 5-6 km ASL, observed by the upward-looking CuBr lidar (Fig.6a), is absent on the other diagram because the Nd:YAG lidar is operated at a slope angle of 58 degrees with respect to the zenith, receiving signals from different spatial domains.

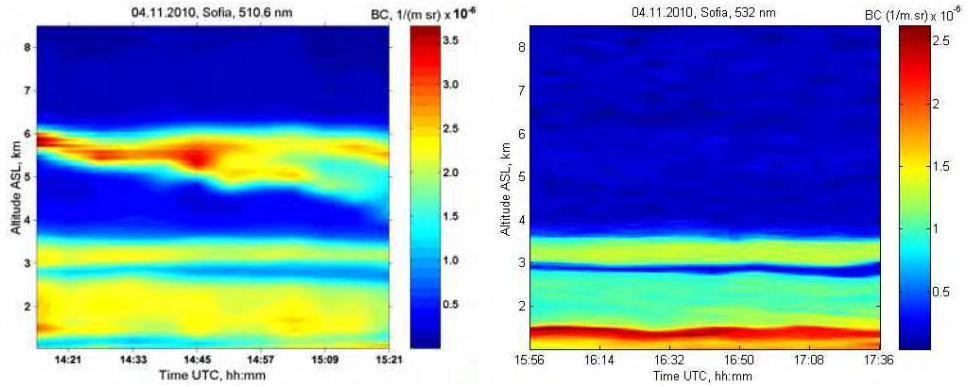

(a) (b)

Fig. 6. Evolution diagrams of the aerosol backscatter coefficient at 510.6 nm (a) and 532 nm (b) as measured by the CuBr and Nd:YAG lidars, respectively, on 04.11.2010.

5.3 Detection of volcanic ashes

The eruption of Eyjafjallajokull volcano in Island on 14 April 2010 offered an opportunity lidar stations, participating in the European Lidar Network, to demonstrate the effectiveness of the lidar sensing for 4-dimensional characterization of the volcanic ash transport. The lidar monitoring of Eyjafjallajokull plumes spreading by the Sofia lidar station started on 18 April 2010 and finished on 25 May 2010 (Grigorov et al., 2011). Results of lidar measurements, performed on 22 April 2010, by using a CuBr lidar at a wavelength of 510.6 nm are given in Fig.7, showing presence of volcanic ash layer positioned at ~2.2 and 3 km altitudes AGL. The observed low limit of the layer frequently remains mixed with the PBL, at about 2-2.5 km altitude AGL.

The lidar observations are presented in two formats: as a single averaged vertical profile of the retrieved backscattering coefficient (Fig.7a) and as a map of the time evolution of the range-corrected lidar signal (RCS) (Fig.7b). The corresponding BSC-DREAM forecast map and the calculated HYSPLIT backward trajectories, proving the origin of the detected aerosols, are presented in Figs.7c and 7d, respectively.

On the plot of the backscattering coefficient, two peaks appear just at the top of the PBL, indicating the presence of aerosol layers at about 2.2 and 3 km altitude AGL. As it can be seen in Fig.7b, where the denser aerosol layers are color coded by orange-red colors, these two layers do not disappear during the whole period of measurement. The forecast map of BSC-DREAM concerning the Sahara dust transport (Fig.7c) shows an atmosphere free of desert dust over the Balkans at that time. In addition, the HYSPLIT backward trajectories (see Fig.7d), corresponding to altitudes of 1.5 km and 3 km AGL, cross the volcano site and/or European countries with volcanic ash atmospheric contamination. So, a conclusion can be drawn, that the detected two aerosol layers are due to the transport of the volcanic ash. The aerosol layers appearing at heights of about 8 km AGL are identified as cirrus clouds.

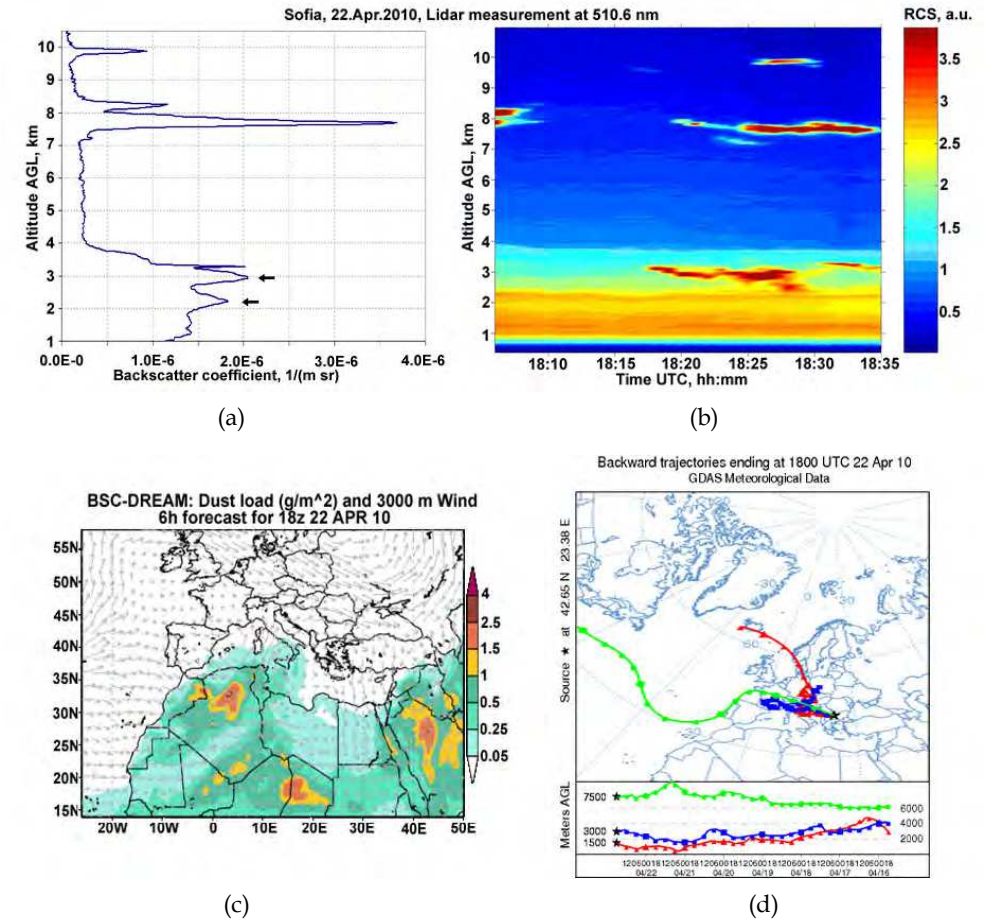

Fig. 7. Results of lidar measurements performed on 22.04.2010: a) averaged vertical profile of the retrieved aerosol backscattering coefficient; b) time evolution of range-corrected lidar signal (RCS); c) BSC-DREAM forecast map of Saharan dust load in the atmosphere; d) backward HYSPLIT air mass trajectories. The two peaks marked with arrows in Fig.7a are volcanic ash layers over Sofia.

5.4 Regular lidar atmospheric measurements

The specialized EARLINET database, resulting from the longtime monitoring of atmospheric aerosols by regular lidar measurements, contains a valuable information for atmospheric processes over Europe (Papayannis et al., 2008). It gives an opportunity for further improvement and validation of atmospheric models and retrieving algorithms applied for climatologic investigations.

Results of lidar measurements carried out by Sofia lidar station on 6 April 2009 are presented in Fig.8a. The color map represents the one-hour evolution of the retrieved

aerosol backscattering coefficient based on lidar profiles with 5 min time averaging in the period 17:00-18:00 UT. The observed multi-layered aerosol structure can be explained analysing the meteorological situation using the corresponding BSC-DREAM dust load forecast map (Fig.8b). It shows that Sofia remains away from the Saharan dust flow. So, we suppose that the two aerosol layers, at 8 km and 9.5 km height, represent cirrus clouds. The layer at 3 km altitude is determined to be a residual aerosol layer, due to the decomposition of the PBL in the evening.

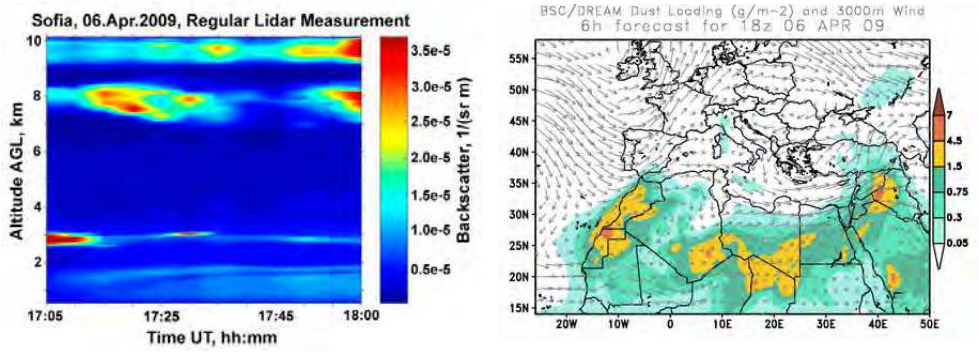

a) b)

Fig. 8. One-hour evolution diagram of the retrieved aerosol backscattering coefficient corresponding to lidar measurements carried out on 6 April 2009 (a) and the BSC-DREAM Saharan dust forecast map (b).

5.5 Correlative space-borne and ground-based lidar measurements

Atmospheric profiling by a network of ground-based lidar stations is an optimal approach for validation of results obtained by space-borne lidars, providing supporting data to fully exploit the information from satellite lidar missions. Such a mission is the Cloud-Aerosol Lidar and Infrared Pathfinder Satellite Observations (CALIPSO). The Cloud-Aerosol LIdar with Orthogonal Polarization (CALIOP), mounted on the CALIPSO satellite, is a Nd:YAG-laser-based lidar specially designed for aerosol and cloud monitoring. Several years correlative ground-based lidar measurements, performed by the EARLINET stations as synchonized with CALIPSO overpasses, contribute to the specialized database, illustrating the potential of the lidar network to provide a sustainable ground-based support for space-borne lidar missions (Pappalardo et al., 2009, 2010).

The Sofia CuBr-lidar group is involved in correlative measurements for CALIPSO since June 2006 (Grigorov et al., 2007). Results of mesurements performed on 28 April 2009 by the ground-based lidar and by the CALIOP lidar are presented in Figs.9a and 9b, respectively.

Vertical red lines on the plots indicate the time of satellite passage over Sofia. On the first plot two aerosol layers can be distinguished. The lower one, located at 1-1.5 km altitude, is due to air convection in the PBL. As seen on the corresponding forecast map of Sahara dust load (Fig.9c), the region covered by the dust flow is in the immediate vicinity of Sofia.

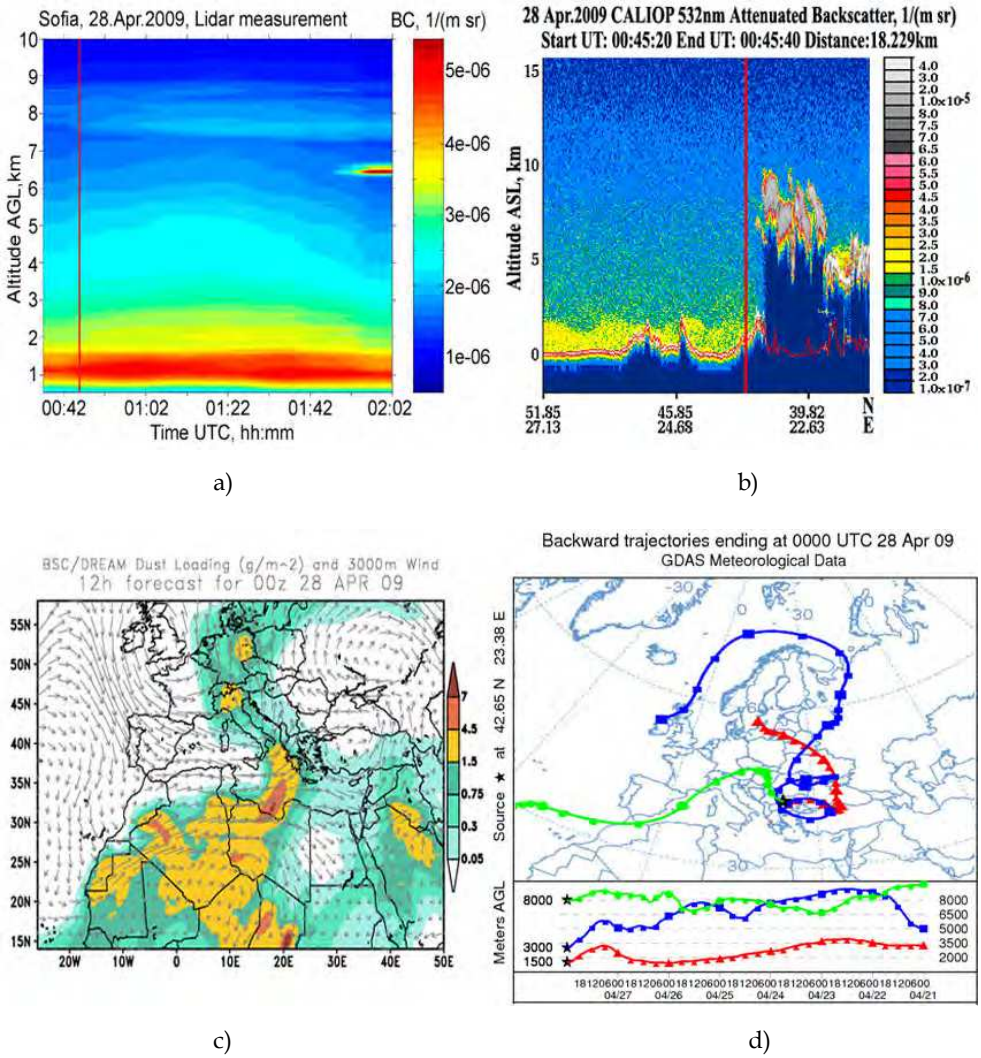

Fig. 9. Sofia-lidar-station and CALIPSO correlative measurements: a) ground-based CuBr lidar data; b) CALIPSO satellite lidar data; c) BSC-DREAM forecast map of Saharan dust load; d) HYSPLIT backward air mass trajectories. The vertical red lines on plots (a) and (b) show the satellite overpass time above Sofia.

Two of the calculated backward air mass trajectories (colored in red and blue on Fig.9d) originate from North Europe. Altough passing over regions loaded with Saharan dust, they are not related to aerosol layers perceptible by the lidar. The green trajectory has an origin above the Atlantic Ocean, indicating for probable transport of humid air which, mixed with the fine Saharan dust particles, can form the aerosol fields appearing at 7.5-8 km height. Similar aerosol layers are present at the same altitude on the plot of CALIPSO satellite lidar

data. The satellite flies over Bulgaria from North-East to South-West. On the CALIOP lidar image, thick aerosol layers occur at 6-9 km altitudes close to the moment of satellite passage over Sofia (see Fig.9b). Those layers, moving from West, are observed by the ground-based lidar in about 1 hour (at ~ 01:50 h UTC, Fig.9a).

6. Multi-wavelength lidar sensing

Lidar sensing in the visible range is typically performed at the second harmonic of the Nd:YAG laser radiation – 532 nm, combined in some lidar systems with the Raman line of the nitrogen molecule at 607 nm. The interval between 532 nm and 1064 nm is not widely used in lidar sounding, mainly because of the dominating usage of Nd:YAG lasers. The US lidar network MPLNET makes use on laser emissions within approximately the same spectral bandwidth (523 nm or 527 nm). As clear from preceding considerations, the metal-vapor lasers cover partially the spectral interval mentioned above. In this Section we consider multi-wavelength lidar probing by MV and Nd:YAG lasers. Some useful theoretical simplifications, providing more correct determination of atmospheric backscattering coefficient profiles, and related experimental results are described and discussed.

6.1 Lidar equations in the case of multi-wavelength sensing by metal vapor lasers

Let us consider for simplicity the case of lidar sensing at two close wavelengths λ_1 and λ_2 (e.g. the ones emitted by a CuBr laser: λ_1=510.6 nm and λ_2=578.2 nm). The case of lidar sensing at more than two wavelengths can be analyzed using similar approach.

Assuming a vertical sounding and replacing further the distance r with the height h, the normalized range-corrected-signal profiles $S_1(h)$ and $S_2(h)$ for both wavelengths are given by

$$S_1(h) = C_1\gamma_1(h)\left[\beta_{a1}(h) + \beta_{m1}(h)\right]T_1(h) \ , \tag{12a}$$

$$S_2(h) = C_2\gamma_2(h)\left[\beta_{a2}(h) + \beta_{m2}(h)\right]T_2(h) \ , \tag{12b}$$

where C_1 and C_2 are the lidar constants; $\gamma_1(h)$ and $\gamma_2(h)$ are the geometrical overlapping functions; $\beta_{a1}(h)$ and $\beta_{a2}(h)$ are the aerosol backscattering profiles; $\beta_{m1}(h)$ and $\beta_{m2}(h)$ are the molecular backscattering profiles; $T_1(h) = \exp[-2\int_0^h \alpha_1(h')dh']$ and $T_2(h) = \exp[-2\int_0^h \alpha_2(h')dh']$ are the atmospheric transmissions. Let us choose some joint reference height h_0 for the two channels and denote by $S_1(h_0)$ and $S_2(h_0)$ the corresponding RCSs, as well as by $\beta_1(h_0)=[\beta_{a1}(h_0)+\beta_{m1}(h_0)]$ and $\beta_2(h_0)=[\beta_{a2}(h_0)+\beta_{m2}(h_0)]$ - the total scattering coefficients. Normalizing the lidar profiles $S_1(h)$ and $S_2(h)$ by their values at $h=h_0$, one can obtain (for $h > h_0$) the dimensionless lidar profiles:

$$L_1(h,h_0) = \frac{S_1(h)}{S_1(h_0)} = \frac{\beta_{a1}(h) + \beta_{m1}(h)}{\beta_1(h_o)}\Gamma_1(h,h_0); \quad \Gamma_1(h,h_0) = \frac{T_1(h)}{T_1(h_0)}\frac{\gamma_1(h)}{\gamma_1(h_0)} \tag{13a}$$

$$L_2(h,h_0) = \frac{S_2(h)}{S_2(h_0)} = \frac{\beta_{a2}(h) + \beta_{m2}(h)}{\beta_2(h_o)}\Gamma_2(h,h_0); \quad \Gamma_2(h,h_0) = \frac{T_2(h)}{T_2(h_0)}\frac{\gamma_2(h)}{\gamma_2(h_0)} \ . \tag{13b}$$

As seen, the normalized lidar profiles do not depend on lidar constants C_1 and C_2 and thus, on some lidar parameters as the emitted powers, receiver sensitivities, etc. The dependence on the overlapping functions can be minimized, if the reference height h_0 is chosen so that $\gamma_1(h) \sim \gamma_2(h) \sim 1$, for $h > h_0$. For non-absorbing atmosphere one could also accept the atmospheric transmissions for λ_1 and λ_2 to be close, i.e. $T_1(h)/T_1(h_0) \sim T_2(h)/T_2(h_0) \sim 1$, and thus, $\Gamma_1(h,h_0) \sim \Gamma_2(h,h_0) \sim 1$. As a result, the normalized profiles $L_1(h,h_0)$ and $L_2(h,h_0)$ will depend on the atmospheric parameters by the profiles of the aerosol and molecular backscattering coefficients. Thus, expressions (13a,b) can be written in the forms:

$$\beta_{a1}(h)+\beta_{m1}(h) = \beta_1(h_0)L_1(h,h_0), \tag{14a}$$

$$\beta_{a2}(h)+\beta_{m2}(h) = \beta_2(h_0)L_2(h,h_0). \tag{14b}$$

The molecular scattering coefficients are expressed by $\beta_{m1}(h) = B_m(h)\lambda_1^{-4}$ and $\beta_{m2}(h) = B_m(h)\lambda_2^{-4}$, where $B_m(h)$ does not depend on λ (Measures, 1984). Their ratio is given by:

$$\theta(\lambda_1,\lambda_2) = \beta_{m2}(h)/\beta_{m1}(h) = (\lambda_1/\lambda_2)^4. \tag{15}$$

In the case of CuBr lidar, $\theta(\lambda_1,\lambda_2) = \theta \approx 0.6$.

By analogy with the molecular scattering, the wavelength dependence of the aerosol backscattering coefficients could be presented in the form:

$$\beta_{a1}(h,\lambda_1) = B_{a1}(h)\lambda_1^{-\eta(h)}; \quad \beta_{a2}(h,\lambda_1) = B_{a2}(h)\lambda_2^{-\eta(h)}, \quad h \ge h_0, \tag{16}$$

where $B_{a1,2}(h)$ and $\eta(h)$ do not depend on the wavelength λ in broad spectral domains. The factor η typically varies within the range $0.57 \le \eta \le 1.8$ for different types of aerosol (Toriumi et al., 1994). Based on the initial supposition stating closeness of the two wavelengths, one can assume

$$B_{a1}(h) \approx B_{a2}(h) = B_a(h) \tag{17}$$

and the ratio $\mu(h,\lambda_1,\lambda_2)$ of backscattering coefficients $\beta_{a2}(h)$ and $\beta_{a1}(h)$ is expressed by a dependence similar to (15):

$$\mu(h,\lambda_1,\lambda_2) = \beta_{a2}(h)/\beta_{a1}(h) = (\lambda_1/\lambda_2)^{\eta(h)}. \tag{18}$$

The vertical profile of $\eta(h)$ used for characterizing aerosol types is given by

$$\eta(h) = \ln[\mu(h,\lambda_1,\lambda_2)]/\ln(\lambda_1/\lambda_2) = \ln[\beta_{a2}(h)/\beta_{a1}(h)]/\ln(\lambda_1/\lambda_2). \tag{19}$$

The parameter $\eta(h)$ as defined in (19) is also called aerosol backscattering-related Ångström exponent (BAE) (Del Guasta, 2002; Kamei et al., 2006). It is involved by analogy with the Ångström exponent (Ångström, 1929, 1964; Shuster et al., 2005) which is normally expressed in terms of aerosol optical depth or extinction. Generally, $\eta(h)$ is a complex function and characteristics of the aerosol particle size distribution and mode volume fractions. In

particular, the BAE values can be influenced by the relative humidity of the atmosphere (Del Guasta & Marini, 2000; Del Guasta, 2002). As calculated from lidar data, the BAE represents a range-resolved function, in contrast to the classical Ångström exponent, thus providing information about the range variations of the aerosol size distribution. In lidars emitting very different wavelengths (say, the first and the second harmonics), the large wavelength differences can cause large variations of the calculated factor $\eta(h)$, depending on shapes and mutual dispositions of the aerosol size distribution modes with respect to the laser wavelengths. This is due to the inequalities $B_{a1}(h) \neq B_{a2}(h)$, indicating for some difference in wavelength dependent scattering mechanisms. It is evident that the conditions (16, 19), when $B_{a1}(h) \approx B_{a2}(h)$ can be satisfied within some defined wavelength domain of bandwidth $\Delta\lambda$, depending on the aerosol size distribution and the aerosol composition. In these cases one can accept some similarity in the aerosol scattering mechanisms. In a clear atmosphere (single mode distribution) $\Delta\lambda$ can practically cover the entire visible and a part of infrared ranges. In the case of multimode size distribution, it can be quite narrower, depending also on the choice of both wavelengths (λ_1, λ_2). The validity of equations (16,19) is of great importance for extracting more and reliable information from the lidar sensing.

It is worth to discuss the opportunities for solving equations (14a,b) for the two wavelengths (λ_1, λ_2). An important requirement here is the normalized lidar profiles $L_1(h,h_0)$ and $L_2(h,h_0)$ to be well distinguished with respect to the noise. As seen, the number of arguments exceeds the number of equations. The parameters $\beta_1(h_0)$ and $\beta_2(h_0)$ could be determined by solving single wavelengths equations (16). The number of arguments could also be reduced using the links of both molecular scattering coefficients $\beta_{m1}(h)$ and $\beta_{m2}(h)$ [see Eq.(15)], as well as applying some well-known models for the standard molecular atmosphere. Using then the model for aerosol backscattering wavelength dependence present above, the number of arguments could also be additionally reduced. The application of this approach is out of the scope of this analysis.

The above analysis shows that the simultaneous multi-wavelength MVL lidar sensing in the mid-visible range, based on the application of the backscattering Ångström exponent profile, is attractive for characterizing vertical aerosol size distribution variations in the submicron and near-micron ranges. The combination with Nd:YAG lidar sensing (1064 nm, 532 nm) is a good approach for a reliable characterization of the most typical atmospheric aerosol loadings.

6.2 Estimation of aerosol-to-molecular scattering proportions

We present below some target experimental results obtained with the CuBr lidar system (Kolarov et al., 1995) emitting two basic wavelengths: λ_1=510.6 nm and λ_2=578.2 nm. To this purpose, let us define the profile of the ratio $R(h,h_0)$ of the two normalized lidar profiles $L_1(h,h_0)$ and $L_2(h,h_0)$:

$$R(h,h_0) = L_2(h,h_0)/L_1[h,h_0], \quad h \geq h_0 . \tag{20}$$

After some transformations, using the simplified expressions (15) we obtain:

$$R(h,h_0) = \left(\frac{\beta_1(h_0)}{\beta_2(h_0)}\right)\frac{\mu(h)\beta_{a1}(h) + \theta\beta_{m1}(h)}{\beta_{a1}(h) + \beta_{m1}(h)} . \tag{21}$$

The variation range of $R(h,h_0)$ for $h \geq h_0$ can be easily estimated. At the reference height h_0 one will obtain $R(h,h_0)$=1. Further, at a proper choice of the reference height h_0 the contribution of the molecular scattering could be neglected for some heights $h \geq h_0$ or $\beta_{a1,2}(h) >> \beta_{m1,2}(h)$ and then, $\mu(h) \sim R(h,h_0)\beta_2(h_0)/\beta_1(h_0)$ as well as $\mu(h_0) \sim \beta_{a2}(h_0)/\beta_{a1}(h_0)$. In the opposite case, one could neglect the contribution of the aerosol scattering with respect to the molecular scattering (Sec.2) above some height h_{max} ($h_{max}>h_0$), where $\beta_{a1,2}(h_{max}) << \beta_{m1,2}(h_{max})$. For this case an approximate estimate for the ratio $R(h_{max},h_0)$ can be also obtained. Using Eq.(21) one will obtain the estimate $R(h>h_{max},h_0) \sim \theta\beta_1(h_0)/\beta_2(h_0) \sim \theta$, if assuming $\beta_1(h_0)/\beta_2(h_0) \sim 1$ for lower heights [see Eqs.(16-19)]. Thus, the range of the height variations of the profile $R(h,h_0)$ will vary approximately within the borders:

$$\theta \leq R(h,h_0) \leq 1 \quad . \tag{22}$$

The use of the ratio $R(h,h_0)$ provides a clear and easy determination of the height h_{max} where one can accept an absence of an aerosol loading. In most of lidar systems it is typically accepted to attach the molecular scattering profile to the range-corrected profiles $S_1(h)$ and $S_2(h)$ at heights above 12-15 km. But, in the presence of intensive daily background this attachment could be even incorrect as the lidar profiles $S_1(h)$ and $S_2(h)$ can contain only noise at higher altitudes. The knowledge of the altitude h_{max} can provide the correct attachment of the molecular profiles in such cases. Moreover, this approach can provide well defined estimates of the aerosol scattering contribution in the point of attachment, if it is lower than h_{max} and thus, an attachment to the molecular scattering in the presence of an aerosol contribution. The measured ratio $R(h,h_0)$ can also be used for estimating the profile of aerosol-to-molecular backscattering coefficients.

Below, we demonstrate some experimental results concerning determination and analysis of calculated profiles of the ratio $R(h,h_0)$ for different aerosol loadings. The plots in Fig.10a present the two normalized lidar profiles: $L_1(h,h_0)$ (curve 1) and $L_2(h,h_0)$ (curve 2) at wavelengths λ_1 and λ_2, respectively. The reference height h_0 is equal to 2 km. Note that both normalized profiles are well distinguished. As expected, the profile for λ_1 is situated in the region of higher values than the profile for λ_2. This is due to the higher molecular scattering for shorter wavelengths. The ratio $R(h,h_{max},h_0)$ is larger than the lower estimate in relation (22) for height up to ~ 4 km. It becomes ~ 0.6 just at this altitude and above, therefore, h_{max} is of the order of 4 km. The attachment of the molecular scattering profile can be implemented at heights above 4 km. As evident, the height h_{max} for attachment of the Rayleigh profiles can be estimated here from lidar data only. This is essential for the accuracy of retrieved aerosol parameters, providing an opportunity to avoid sometimes the application of complicated set of calibration procedures (Bösenberg & Hoff, 2007).

The results in Fig.10b correspond to the case, when the calculated ratio $R(h,h_{max},h_0)$ is higher and approximately equal to ~ 0.8 in a large region of altitudes up to 10 km. This case can be characterized as a case of significant aerosol loading up to altitudes of 10 km. It must be noted that the both normalized profiles are approximately parallel and well distinguished as well. Some additional small aerosol contribution above 6km are well seen also in the profile of the ratio $R(h,h_{max},h_0)$. This fact could be explained by some changes of the aerosol size distribution at these altitudes, due to the presence of additional thin cloud loading having different aerosol scattering structure. For lower heights, the ratio $R(h,h_{max},h_0)$ tends to unity as expected. As seen, the ratio $R(h,h_{max},h_0)$ becomes very informative when the two

wavelengths are closely disposed (but at well distinguished lidar profiles) so the uncertainties introduced by the parameters of two lidar channels can be minimized (see Eqs.13a,b). In this sense, the application of MVL in lidar atmospheric probing can be substantial for improving the measurement accuracy.

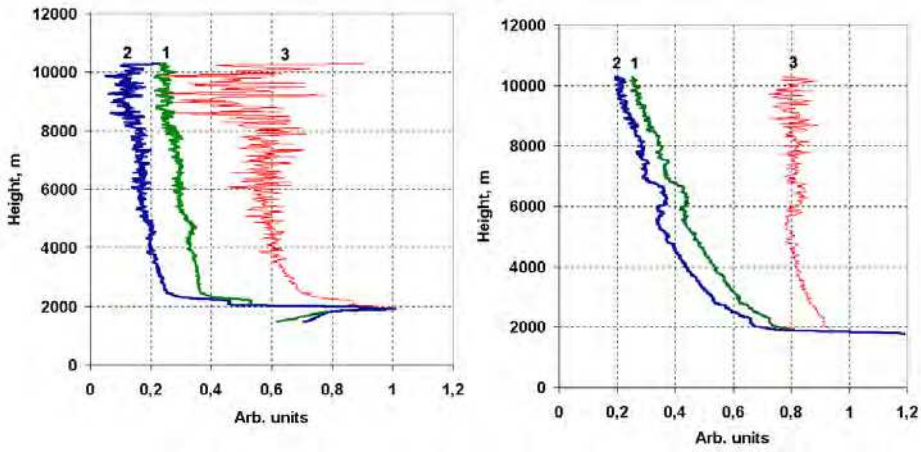

a) b)

Fig. 10. a) Normalized lidar profiles 1 and 2 (on both wavelengths, respectively) and the calculated ratio $R(h,h_{max},h_0)$ 3, measured in a clear atmosphere on 10.07.2008; b) Normalized lidar profiles 1 and 2 and the calculated ratio 3, measured in mixed (aerosol and molecular scattering) atmosphere on 17.07.2008.

6.3 Two-wavelength lidar probing of aerosol mode fractions over complex terrain

Results of lidar observations on atmospheric aerosols over a complex terrain (Fernando, 2010), representing adjoining city-, plain-, and mountain zones in Sofia region, are described below. A residential city zone is located along with the first 2 kilometers of the laser beam path. The distance range 2 - 5 km covers city outskirts and suburbs (plain zone) and the one from 5.5 km to about 9 km covers the mountain foot, slope, and ridge (mountain zone).

Lidar measurements (Fig.11) are carried out simultaneously at wavelengths 1064 nm and 532 nm (Peshev et al., 2011). Range profiles of evaluated aerosol backscattering coefficients (molecular component subtracted) on 28.01.2008, averaged over the period of measurements (17:10 h – 18:15 h GMT), are presented in Fig.12a. Over the plain area, the backscattering coefficient at 532 nm is permanently higher than the one at 1064 nm, starting with a ratio of about 1.5-2 and gradually decreasing to equalization close to the interface between the plain and mountain. Humps observed at the initial parts of the two profiles (city zone) are identified to be due to increased anthropogenic aerosol emissions. For the rest of the plain zone, profiles are quite smooth, without differentiated bulges.

Over the mountain zone, the situation is inverted – the backscattering at 1064 nm exceeds the one at 532 nm, both having values considerably higher than those for the plain zone, denoting

presence of dense aerosol layers, most probably - water aerosol (fog or orographic clouds near the surface). The available meteorological data for the day support this conclusion.

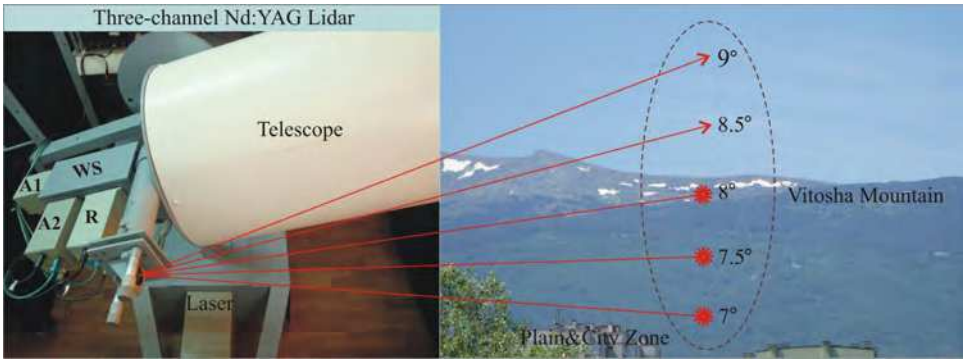

Fig. 11. Schematic view of the lidar experiment over complex terrain; WS – wavelength separator; A1 and A2 – aerosol channels at 1064 nm and 532 nm, respectively; R – Raman channel at 607 nm.

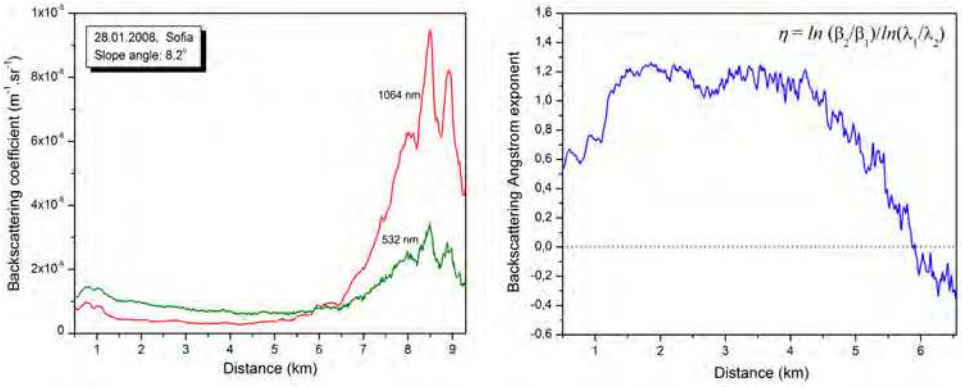

a) b)

Fig. 12. a) Time-averaged profiles of aerosol backscattering coefficient at the two wavelengths of measurement; b) Backscattering-related Ångström exponent profile.

The backscatter-related Ångström exponent defined in Eq.(19) is used as a qualitative indicator of aerosol particle properties. In Fig.12b, the range profile of BAE is presented, corresponding to aerosol backscatter profiles shown on Fig.12a. As one can see, the values of η vary within the range 0.5-1.25 for distances of up to 5 km (plain zone). These values indicate for prevalence of the fine-mode aerosol particle fraction, most probably of anthropogenic origin, as typical for urban areas under dry atmospheric conditions.

Around the plain-to-mountain interface zone located about 5.5 km away from the lidar station, BAE values approach zero indicating for prevailing contribution of the coarse-mode aerosol fraction.

The BAE takes gradually decreasing negative values for distances corresponding to the mountain zone (Fig.12b). Negative values of the extinction-related or backscatter-related Ångström exponent (Kamei, 2006; Lu, 2011; Guerrero-Rascado, 2009) occur in cases of large aerosol particles in the over-micron size range (e.g. large water droplets, ice particles, volcanic or fire ashes, partcle aggregates, etc.), as well as in case of large mode volume fractions of coarse aerosols with respect to those of fine aerosols. In these cases, the backscattering at longer wavelengths dominates over the one at shorter wavelengths, especially for substantially different wavelengths, as in Fig.12b.

7. Conclusions

Various lidar technologies have been developed since the first lidar demonstration more than 40 years ago. In this chapter we presented some of the basic applications of lidars in the atmospheric research. The high informativity of lidar probing is due to the strong interaction of optical waves with atmospheric particles – aerosols and molecules, combined with range-resolved acquisition of lidar signals. The fast spread of lidars all over the world in the last two decades led to their organizing in regional lidar networks as EARLINET (Europe), MPLNET (USA), AD-Net (Japan), etc., integrated now in the Global lidar network (GALION). As lidars are practically the only instruments for high resolution vertical atmospheric profiling, their further improvement is one of the most important tasks for the lidar community. One of the ways to enhance the quality of lidar output information and its significance for the global and regional atmospheric monitoring is the creation of complex multispectral lidar systems, capable to provide more detailed and reliable data for the retrieval of aerosol optical, microphysical, and radiative properties, etc. This approach requires the development of novel more effective inverse algorithms, as well. It is also expected the future lidar networks to operate in a close cooperation with other existing networks as the sun-photometer network, ground-level in-situ aerosol monitoring networks, satellite measurements (lidar and multispectral radiometers), radars, etc. The synergy resulting from such cooperation was demonstrated in a large number of experiments. The expected increase of the lidar station density all over the world is a good indication for their great significance in analysing local and global atmospheric processes and trends. In this connection we note the European project ACTRIS (Aerosols, Clouds, and Trace gases Research InfraStructure Network (www.actris.net)). Started in 2011 under 7-th Framework Program, it integrates the EARLINET, EUSSAR, CLOUDNET, and a new trace gas network into single-coordinated ground-based networks, with monitoring impact on the climate changes, air quality, and long-term transport of pollutants.

8. Acknowledgments

The results described here were funded partly by the Bulgarian National Science Fund under projects Ph-63, Ph-447, Ph-811 and the European Commission under the project EARLINET-ASOS, grant RICA-025991 EC FP6. The authors thank the NOAA Air Resources Laboratory (ARL) for the provision of the HYSPLIT backward trajectories. We also thank the Barcelona Supercomputing Center for Dust Regional Atmospheric Model (DREAM) and for the provision of Saharan dust forecast maps.

9. References

Ångström, A., (1929). On the atmospheric transmission of Sun radiation and on dust in the air, *Geogr. Ann.,* Vol.11, pp.156–166.

Ångström, A., (1964). The parameters of atmospheric turbidity, *Tellus*, Vol. 16, pp.64–75.

Arshinov, Yu.; Bobrovnikov, S.; Zuev, V. & Mitev, V. (1983). Atmospheric temperature measurements using a pure rotational Raman lidar, *Appl. Optics*, Vol.22, pp.2984-2987.

Astadjov, D.; Vuchkov, N. & Sabotinov, N. (1988). Parametric study of the CuBr laser with Hydrogen additivies, *IEEE J.Quant.Electron.*, Vol. QE-24, pp.1927-1935.

Böckmann, C.; Grigorov, I.; Hågård, A.; Horvat, M.; Iarlori, M.; Komguem, L.; Kreipl, S. & Frioud, M. (2004). Aerosol lidar intercomparison in the framework of the EARLINET project. 2. Aerosol backscatter algorithms, *Appl. Opt.*, Vol. 43 (4), pp. 977-989.

Bösenberg, J., et al. (2003). EARLINET: A European Aerosol Research Lidar Network to establish an aerosol climatology, Rep. 348, Max Planck Inst. für Meteorol., Hamburg, Germany.

Bösenberg, J. & Hoff, R., lead authors (2007). *Plan for the implementation of the GAW Aerosol Lidar Observation Network GALION*, GAW No.178, WMO, Hamburg, Germany. Available from ftp://ftp.wmo.int/Documents/PublicWeb/arep/gaw/gaw178-galion-27-Oct.pdf

Del Guasta, M. & Marini, S. (2000). On the retrieval of urbanaerosol mass concentration by a 532 and 1064 nm LIDAR. *J. Aeros. Sci.,* Vol.31, No.12, pp.1469–1488.

Del Guasta, M. (2002). Daily cycles in urban aerosols observed in Florence (Italy) by means of an automatic 532–1064 nm LIDAR. *Atm. Environ.,* Vol.36, No.17, pp.2853–2865.

Draxler, R.R. & Hess, G.D. (1998). An overview of the HYSPLIT_4 modeling system of trajectories, dispersion, and deposition. *Aust. Meteor. Mag.*, Vol. 47, 295-308.

Draxler, R.R. & Rolph, G.D. (2011). HYSPLIT (HYbrid Single-Particle Lagrangian Integrated Trajectory) Model access via NOAA ARL READY Website (http://ready.arl.noaa.gov/HYSPLIT.php). NOAA Air Resources Laboratory, Silver Spring, MD.

Fernald F., Analysis of atmospheric lidar observations: some comments, *Appl.Opt.* (1984) 23, (5), pp.852-853

Fernando, H. J. S. (2010). Fluid dynamics of urban atmospheres in complex terrain, *Ann. Rev. Fluid Mech.* Vol.42, pp.365-389

Gagarin, S.; Kalinkevich, A.; Kolarov, G.; Kutuza, B.; Mikhalev, M.; Mitsev, Ts.; Stoykova, E.; Stoyanov, D.; Ferdinandov, E. & Khaimov S. (1987). Investigation of the atmosphere by using microwave radiometric and lidar signals, *Atm. Ocean Optics*, Vol. 23, No. 2, pp. 121-129.

Gagliardi, R.M. & Karp, S. (1976). *Optical Communications*, Wiley, New York, USA.

Grigorov, I.V. & Kolarov, G.K. (2007). Measurements of atmospheric parameters using aerosol lidar, *JOAM*, Vol. l9, No. 11, pp. 3549-3552.

Grigorov, I.; Kolarov, G. & Stoyanov, D. (2009). Lidar remote monitoring of aerosol dust layers over Sofia, *Proc. ICEST'2009 XLIV Int. Scientific Conf.,* pp. 563-566.

Grigorov, I.; Kolarov, G. & Stoyanov, D. (2010). Remote monitoring of aerosol layers over Sofia in the frame of EARLINET-ASOS project, *AIP Conference Proceedings* ,Vol. 1203, 2010, DOI: 10.1063/1.3322514, pp. 585-590

Grigorov, I.; Stoyanov, D. & Kolarov, G. (2011). Lidar observation of volcanic dust layers over Sofia, *Proc. SPIE,* Vol. 7747, paper # 77470R.

Guerrero-Rascado, J. L.; Olmo, F.J.; Avilés-Rodríguez, I.; Navas-Guzmán, Pérez-Ramírez, F., Lyamani, D. H. & Arboledas, L. A. (2009). Extreme Saharan dust event over the southern Iberian Peninsula in september 2007: active and passive remote sensing from surface and satellite, *Atmos. Chem. Phys.*, Vol. 9, pp. 8453-8469, doi:10.5194/acp-9-8453-2009.

Kallos, G. et al. (1997). The regional weather forecasting system SKIRON: An overview, in Proceedings of the Symposium on Regional Weather Prediction on Parallel Computer Environments, edited by G. Kallos, V. Kotroni, and K. Lagouvardos, pp. 109–122, Univ. of Athens, Athens, Greece.

Kamei, A.; Sugimoto, N., Matsui, I., Shimizu, A. & Shibata, T. (2006). Volcanic Aerosol Layer Observed by Shipboard Lidar over the Tropical Western Pacific. *SOLA,* Vol.2, 001-004, doi:10.2151/sola.2006-001

Kim, J.J. (1991). Metal vapour lasers: a review of recent progress, *Opt. Quant. Electronics*, vol.23, pp.S469-S476.

Klett, J. (1981). Stable analytical inversion solution for processing lidar returns, *Appl.Opt.*, vol. 22, pp.211-220.

Kolarov, G.; Stoyanov, D.; Mitsev, Ts. & Againa, Ts. (1988). Sounding of the atmospheric aerosol by a lidar on copper vapour laser, *Atm. Optics*, Vol. 1, No. 6, pp. 125-126.

Kolarov, G.; Grigorov, I. & Stoyanov, D. (1995). Estimation of the ratio of aerosol to molecular backscattering by two closely disposed wavelengths using CuBr lidar sounding (510.6 nm, 578.2 nm), *Proc. SPIE,* Vol. 7027, paper # 702710.

Kovalev, V.A. & Eichinger, W.E. (2004). *Elastic Lidar: Theory, Practice, and Analysis Methods*, Wiley, New York, USA.

Lu, X; Jiang, Y.; Zhang, X.; Wang X. & Spinelli, N. (2011). Two-wavelength lidar inversion algorithm for determination of aerosol extinction-to-backscatter ratio and its application to CALIPSO lidar measurements, *J. Quantat. Spectr. & Radiat. Transf.*, Vol. 112, pp. 320–328.

Measures, R.M. (1984). *Laser Remote Sensing*, Wiley, New York, USA.

Mitzev, Tz.; Grigorov, I.; Kolarov, G. & Lolova, D. (1995). Investigation of transborder pollution by combining remote lidar sounding and stationary gas sampling, Proc.SPIE, vol.2506, pp.310-318.

Nickovic, S.; Papadopoulos, A.; Kakaliagou, O. & Kallos, G. (2001). Model for prediction of desert dust cycle in the atmosphere, *J. Geophys. Res.*, vol. 106, pp. 18,113– 18,129.

Ozsoy, E.; Kubilay, N.; Nickovic, S. & Moulin, C. (2001). A hemispheric dust storm affecting the Atlantic and Mediterranean (April 1994): Analyses, modelling, ground-based measurements and satellite observations, *J. Geophys. Res.*, Vol. 106, pp. 18, 439–18,460.

Pappalardo, G. et al. (2009). The EARLINET Contribution to the EarthCARE Mission, *EarthCARE 2009 Workshop*, 15.July.2009.

Pappalardo, G. et al. (2010). EARLINET correlative measurements for CALIPSO: First intercomparison results., *J. Geophys. Res.-Atmospheres,* Vol. 115, D00H19, doi: 10.1029/2009JD012147

Papayannis A. et al. (2008). Systematic lidar observations of Saharan dust over Europe in the frame of EARLINET (2000-2002), *J. Geophys. Res.*, Vol. 113, D10204.

Perez, C.; Nickovic, S.; Baldasano, J.M.; Sicard; M.; Rocadenbosch, F. & Cachorro, V. (2006a) . A long Saharan dust event over the western Mediterranean: Lidar, Sun photometer observations, and regional dust modelling *J. Geophys. Res.*, Vol. 111, D15214, doi:10.1029/2005JD006579.

Perez, C.; Nickovic, S.; Pejanovic, G.; Baldasano, J.M. & Ozsoy, E. (2006b). Interactive dust-radiation modeling: A step to improve weather forecasts, *J. Geophys. Res.*, Vol. 111, D16206, doi:10.1029/2005JD006717, 2006

Peshev, Z. Y.; Deleva, A. D., Dreischuh, T. N. & Stoyanov, D.V. (2010). Lidar measurements of atmospheric dynamics over high mountainous terrain, *AIP Conf. Proc.*, Vol. 1203, pp. 1108-1113.

Peshev, Z.Y.; Deleva, A.D., Dreischuh, T.N. & Stoyanov, D.V. (2011) Dynamical characteristics of atmospheric layers over complex terrain probed by two-wavelength lidar, *Proc. SPIE*, Vol. 7747, paper # 77470U.

Schuster, G. L.; Dubovik, O. & Holben, B. N. (2006). Angstrom exponent and bimodal aerosol size distributions, *J. Geophys. Res.*, Vol.111, D07207.

Stoilov, V.; Astadjov, D.; Vuchkov, N. & Sabotinov, N. (2000). High spatial intensity 10 W-CuBr laser with hydrogen additives, *Opt. Quant. Electr.*, vol.32, pp. 1209-1217.

Stoyanov, D.; Donchev, A.; Kolarov, G. & Mitsev, Ts. (1988). Copper and gold vapour laser radar for troposphere and stratospheric studies, *Atm. Optics*, Vol. 1, pp. 109-116.

Stoyanov, D. (1997). Counting of overlapped photon detector single pulses by analog/digital sampling and deconvolution, *Opt. Eng.*, Vol. 36, pp. 210-216.

Stoyanov D.; Vankov, O. & Kolarov, G. (2000). Measuring the arrival times of overlapped photo-events, *Nucl. Instrum. Methods Phys. Res. A*, Vol. 449, pp. 555-567.

Toriumi, R.; Tai, H.; Okumura, H. & Takeuchi, N. (1994). Wavelength dependence of aerosol optical parametres measuredby a tunable lidar, Abstracts of papers, 17th ILRC, July 25-29, Sendai, Japan, pp.91-92.

Weitkamp, C., Ed. (2005). *Lidar: Range-Resolved Optical Remote Sensing of the Atmosphere*, Springer Series in Optical Sciences, New York, USA.

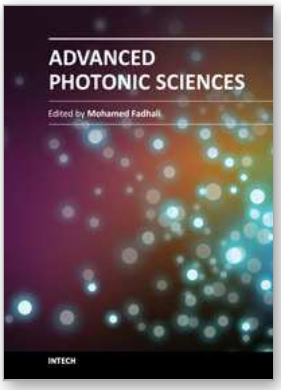

Advanced Photonic Sciences

Edited by Dr. Mohamed Fadhali

ISBN 978-953-51-0153-6
Hard cover, 374 pages
Publisher InTech
Published online 21, March, 2012
Published in print edition March, 2012

The new emerging field of photonics has significantly attracted the interest of many societies, professionals and researchers around the world. The great importance of this field is due to its applicability and possible utilization in almost all scientific and industrial areas. This book presents some advanced research topics in photonics. It consists of 16 chapters organized into three sections: Integrated Photonics, Photonic Materials and Photonic Applications. It can be said that this book is a good contribution for paving the way for further innovations in photonic technology. The chapters have been written and reviewed by well-experienced researchers in their fields. In their contributions they demonstrated the most profound knowledge and expertise for interested individuals in this expanding field. The book will be a good reference for experienced professionals, academics and researchers as well as young researchers only starting their carrier in this field.

INTECH
open science | open minds

InTech Europe
University Campus STeP Ri
Slavka Krautzeka 83/A
51000 Rijeka, Croatia
Phone: +385 (51) 770 447
Fax: +385 (51) 686 166
www.intechopen.com

InTech China
Unit 405, Office Block, Hotel Equatorial Shanghai
No.65, Yan An Road (West), Shanghai, 200040, China
中国上海市延安西路65号上海国际贵都大饭店办公楼405单元
Phone: +86-21-62489820
Fax: +86-21-62489821